

The molecular basis of the interactions between synthetic retinoic acid analogues and the retinoic acid receptors

Hesham Haffez,^{a,b,c,d} David R. Chisholm^a, Ehmke Pohl,^{a,b} Christopher Redfern^c Roy Valentine^e and Andrew Whiting^{a*}

^aDepartment of Chemistry Durham University, South Road, Durham, DH1 3LE, UK.

^bDepartment of Biosciences Durham University, South Road, Durham DH1 3LE, UK.

^cNorthern Institute for Cancer Research, Medical School, Newcastle University, Newcastle upon Tyne, NE2 4HH, UK.

^dDepartment of Biochemistry and Molecular Biology, Pharmacy College, Helwan University, Cairo, Egypt.

^eHigh Force Research Ltd., Bowburn North Industrial Estate, Bowburn, Durham, DH6 5PF, UK.

Table of Contents

Biochemical model of the TR-FRET binding assay	2
Calculated conformer distributions of ATRA, 9CRA, EC23, EC19, EC23Me and EC19Me	6
Statistical analysis of ATRA docking conformation clustering	14
Additional hydrophobic interaction images	15
Additional hydrogen bonding interaction images.....	22
References.....	26

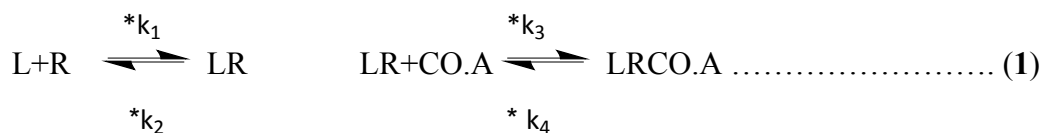
Biochemical model of the TR-FRET binding assay

The readout of the Lanthascreen TR-FRET binding assay is based on a Forster resonance energy transfer (FRET) signal generated from the interaction between a terbium-labelled anti-glutathione-S-transferase (GST) antibody and a fluorescein-labelled coactivator peptide. The RAR ligand-binding domain (LBD) is a GST fusion protein and interaction between the LBD and the fluorescein-labelled coactivator peptide is driven by the binding of ligand to the LBD, and detected by the FRET signal from the terbium/fluorescein interaction when the terbium-labelled anti-GST binds the LBD fusion protein. The output of the assay thus relies on two binding interactions: ligand with LBD, and ligand-bound LBD with the coactivator peptide. As both interactions may be affected by the fit of ligand to the binding pocket of the LBD, we used the biochemical pathway simulator COPASI¹ to build a simple model of how the FRET signal output in the assay will vary according to differential changes in the kinetics of the two binding interactions. Reactions were modelled deterministically using mass-action kinetics described by ordinary differential equations (ODE) within COPASI.¹

The species in the model are:

Ligand (L), Receptor (R), Ligand-Receptor complex (LR), Co-activator (Co.A) and Ligand-Receptor Co-activator complex (LRCo.A).

The model is based on two reversible reactions



* Where k_1 , k_2 and k_3 , k_4 are the rate constants controlling the rate of LR and LR.CO.A complex formation, respectively.

Thus:

$$k_1 [L] [R] = k_2 [LR]$$

$$\text{And } k_1/k_2 = [L] [R]/[LR]$$

$$\text{Similarly } k_3 [LR] [CO.A] = k_4 [LRCO.A]$$

$$\text{And therefore } k_3/k_4 (K_d') = [LR] [CO.A]/[LRCO.A] \dots\dots\dots (2)^2$$

All species concentrations were expressed as $\mu\text{mol.L}^{-1}$ and changed during the simulation by dynamic evaluation of ODEs

Starting concentrations were;

$$L = 10 \mu\text{mol. L}^{-1} \text{ to } 0.03 \text{ nmol. L}^{-1}$$

$$R = 0.0035 \mu\text{mol. L}^{-1} \text{ (defined by the assay formulation)}$$

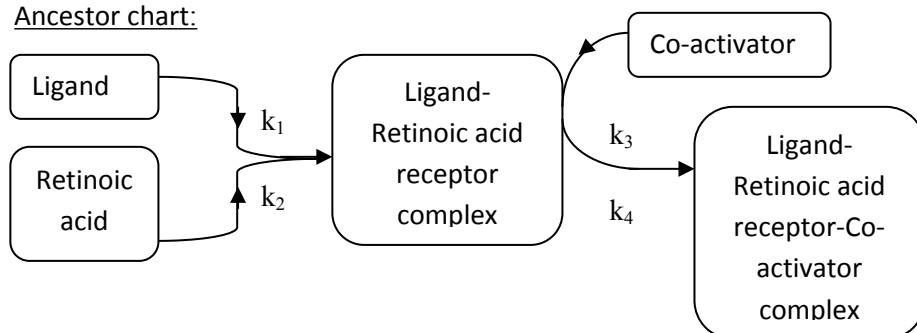
$$CO.A = 30 \mu\text{mol. L}^{-1} \text{ (defined by the assay formulation)}$$

$$LR = 0 \mu\text{mol. L}^{-1}$$

$$LRCo.A = 0 \mu\text{mol. L}^{-1}$$

Steady states for LRCo.A were derived from the range of ligand starting concentrations ($10 \mu\text{mol. L}^{-1}$ to $0.03 \text{ nmol. L}^{-1}$) using the Steady State and Parameter Scan functions within COPASI.

Ancestor chart:



This model enables us to assess the effect of different rate constants and varying ligand concentration on the formation of the final ternary complex that is the read-out from the Lanthascreen TR-FRET assay. The two coupled equilibria given in **1** are controlled by the four rate constants k_1 - k_4 . Rate constants from analogous ligand-nuclear receptor systems^{3,4} were used as the starting point for calculating the EC_{50} (half maximal effective concentration) for ATRA. These rate constants ($k_1 = 0.6 \mu\text{mol. L}^{-1}$, $k_2 = 0.1 \text{ min}^{-1}$, $k_3 = 0.014 \mu\text{mol. L}^{-1}$ and $k_4 = 0.2 \text{ min}^{-1}$) were then altered individually or together to model different possible scenarios. The simulation results show that the k_1/k_2 ratio, reflecting the affinity of ligand for LBD, directly affects EC_{50} values, while alteration in k_3/k_4 , reflecting the affinity of co-activator for the ligand-LBD complex (LR), changes both the EC_{50} and upper asymptote (Fig. 2).

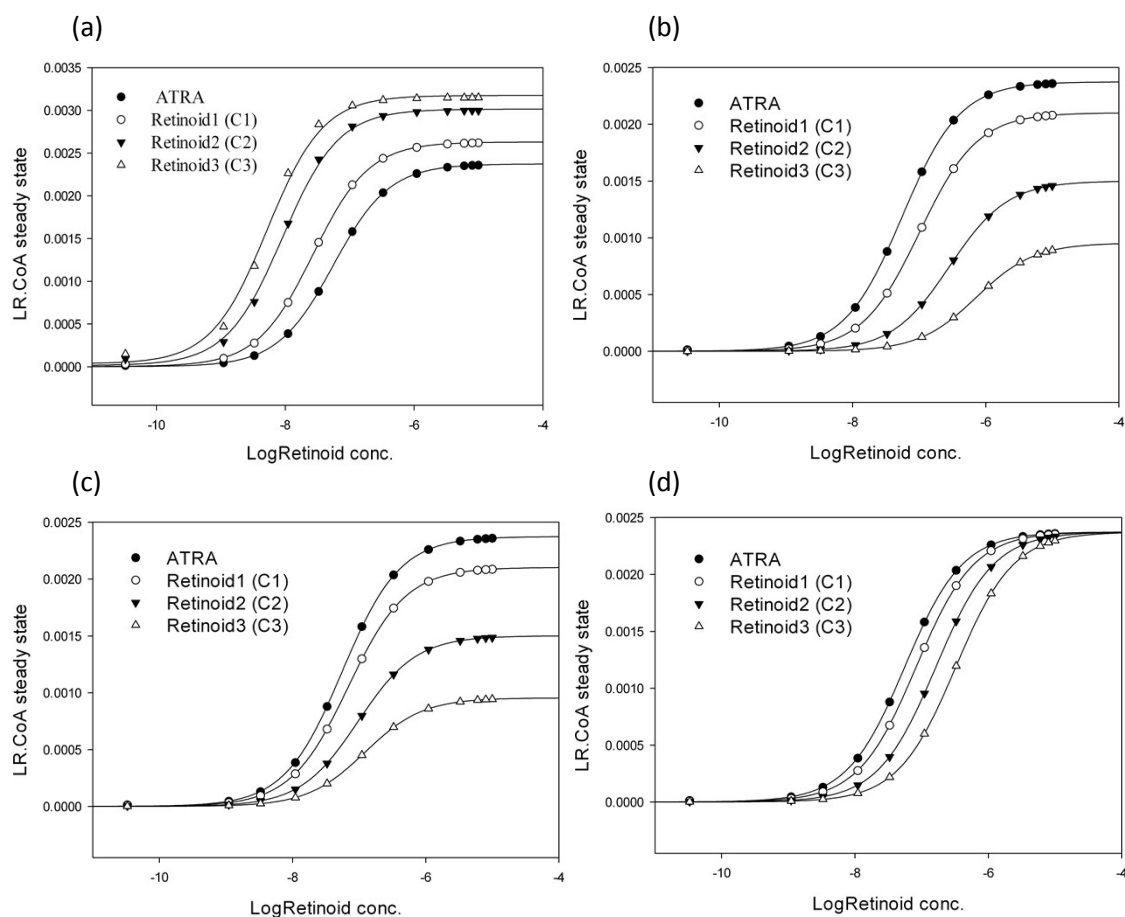


Figure 1: Biochemical simulation analysis of TR-FRET assay using COPASI software assuming 3 different retinoid compounds to show the effect of changes in k_1/k_2 and k_3/k_4 values on EC_{50} . (a) High ligand-receptor binding affinity and high induction of co-activator binding ($k_1/k_2 = 10, 20, 30$ and $k_3/k_4 = 0.1, 0.2, 0.3$) leads to low EC_{50} values in the range of 9-27 nM for the virtual compounds C1, C2, C3 which are hypothetical ATRA analogues with increasing k_1/k_2 and k_3/k_4 values. Increasing both ratios leads to decreased EC_{50} values and upper asymptotes (b) Lower ligand-receptor binding affinity and co-activation binding ($k_1/k_2 = 4, 2, 1$ and $k_3/k_4 = 0.05, 0.025, 0.0125$) leads to higher EC_{50} values in the range of 102-729 nM for the virtual compounds C1, C2, C3 which are hypothetical ATRA analogues with lower k_1/k_2 and k_3/k_4 values. Increasing both ratios leads to decreased EC_{50} values upper asymptotes (c) No change in ligand-receptor binding affinity and lower co-activation binding ($k_1/k_2 = 6$ and $k_3/k_4 = 0.05, 0.025, 0.0125$) leads to higher EC_{50} values in the range of 102-729 nM for the virtual compounds C1, C2, C3 which are hypothetical ATRA analogues with lower k_1/k_2 and k_3/k_4 values. Increasing both ratios leads to decreased EC_{50} values and upper asymptotes (d) Lower ligand-receptor binding affinity and no change in co-activation binding ($k_1/k_2=4, 2, 1$ and $k_3/k_4 = 0.07$) leads to higher EC_{50} values in the range of 82.6-324 nM for the virtual compounds C1, C2, C3 which are hypothetical ATRA analogues with lower k_1/k_2 and k_3/k_4 values. Increasing both ratios leads to decreased EC_{50} values only. Graphs were produced by SigmaPlot based on steady state calculated by COPASI¹ and using the 3-parameter sigmoidal curve $f = \min + (\max - \min)/(1+10^{-(\log EC_{50} - x)})$ to fit the output.

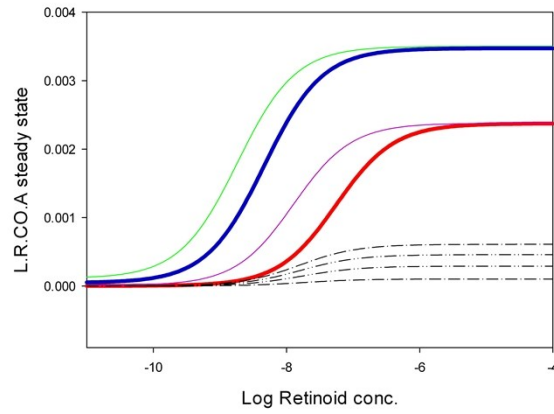
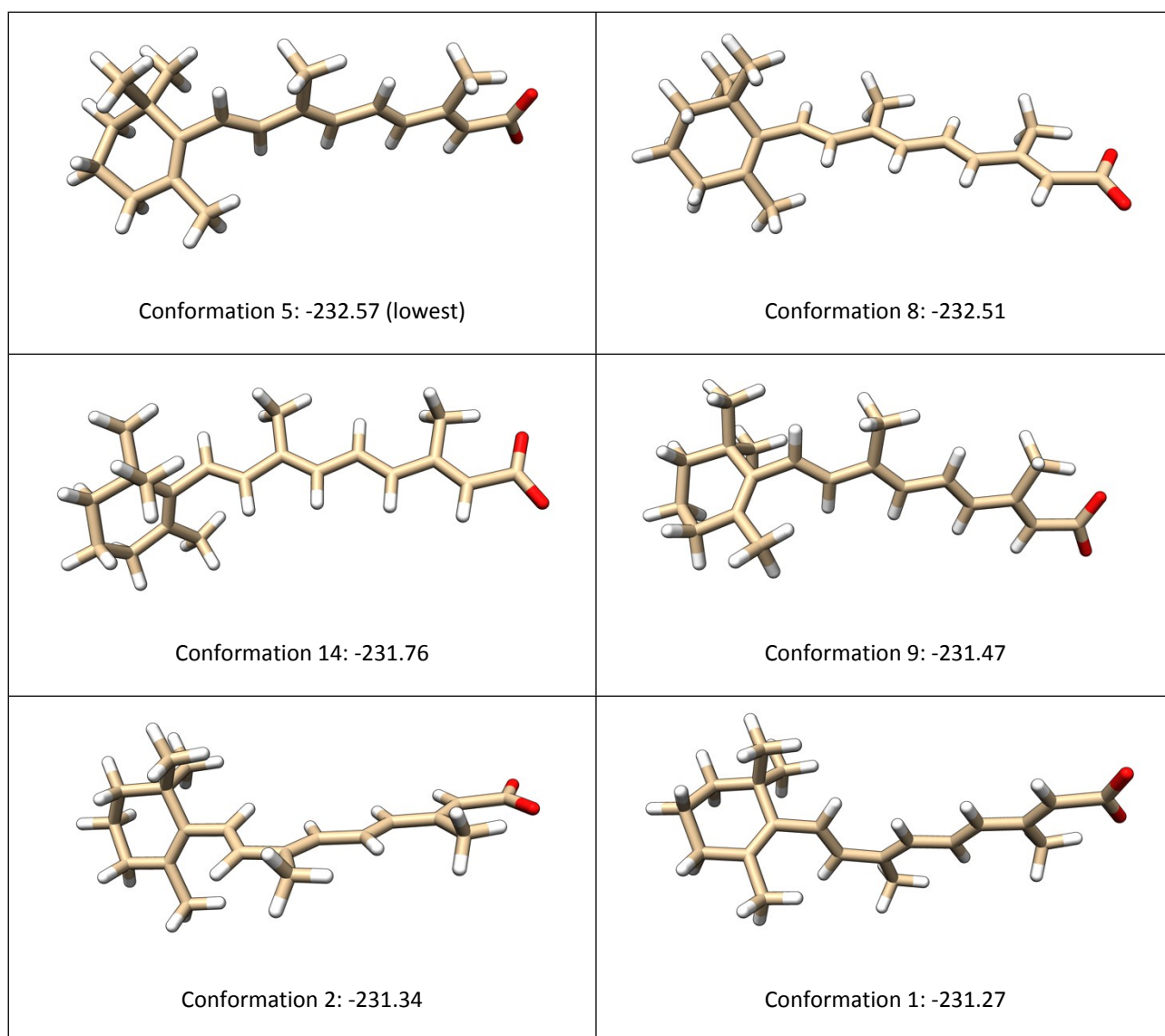


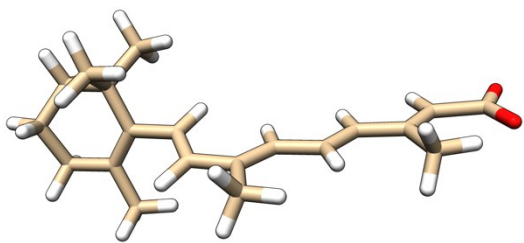
Figure 2: Summary of biochemical simulations for the TR-FRET assay using COPASI assuming 7 different retinoid compounds to show the relationships between ligand-receptor-coactivator affinity, EC_{50} and upper asymptote. All these compounds have lower EC_{50} compared to ATRA (red line) with different scenarios, green line (both k_1/k_2 and k_3/k_4 are higher than ATRA), blue line (similar k_1/k_2 and higher k_3/k_4 than ATRA), pink line (higher k_1/k_2 and similar k_3/k_4 to ATRA), black dashed lines (higher k_1/k_2 and lower k_3/k_4 than ATRA). Graphs were produced by SigmaPlot based on steady state calculated by COPASI¹ and using the 3-parameter sigmoidal curve $f = \min + (\max - \min) / (1 + 10^{(\log EC_{50} - x)})$ to fit the output.

Calculated conformer distributions of ATRA, 9CRA, EC23, EC19, EC23Me and EC19Me

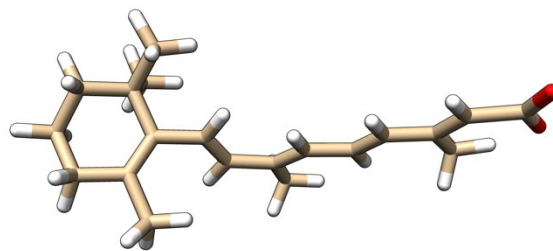
Tables 1-6 show the calculated conformer distributions of ATRA, 9CRA, EC23, EC19, EC23Me and EC19Me. The calculation suggests that ATRA exists in a series of conformations with *s-cis* and *s-trans* arrangements of the polyene chain and the differences in energy between the lowest and highest energy is only around 15 kJ/mol. 9CRA exhibits a similarly large range of conformations, although the higher energy conformations did not appear to be complementary towards the RAR LBPs. As with ATRA, the difference in energy between the lowest and highest energy conformations is only around 19 kJ/mol. EC23, EC19, EC23Me and EC19Me all exhibited only a few conformations, each within 0.5 kJ/mol.

Table 1: Conformer distribution of ATRA in order of lowest energy. Distribution was calculated using the AM1 forcefield, and energies are shown from this calculation. The results were further validated at a higher level of theory (HF, STO-3G), and no obvious differences were exhibited. Energies are expressed in kJ/mol, and were calculated using Spartan 14. Each of these calculated conformations was used as a starting point for the docking process.

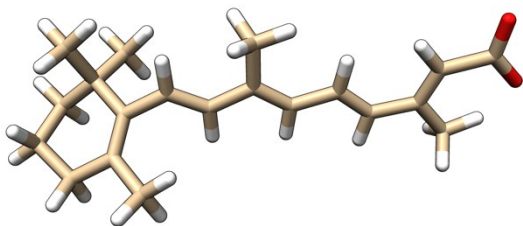




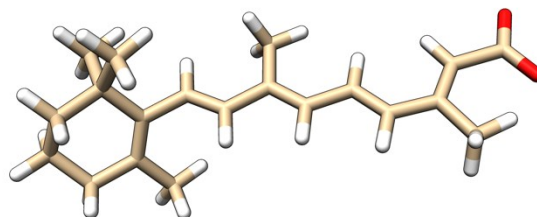
Conformation 3: -230.48



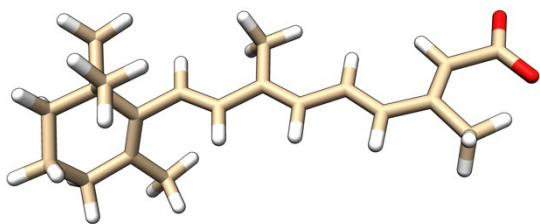
Conformation 4: -230.47



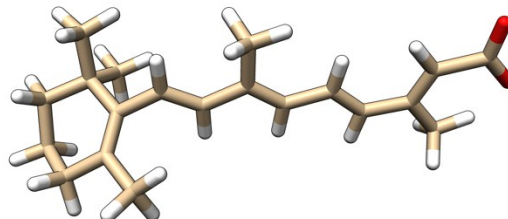
Conformation 12: -229.13



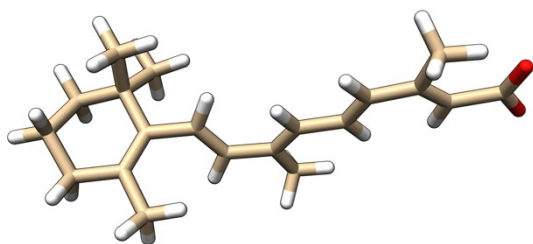
Conformation 13: -229.12



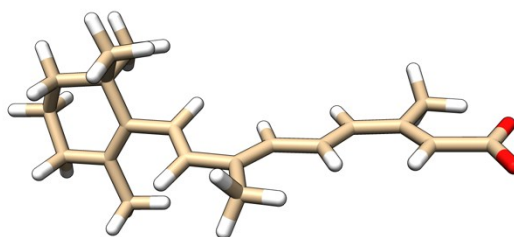
Conformation 16: -228.38



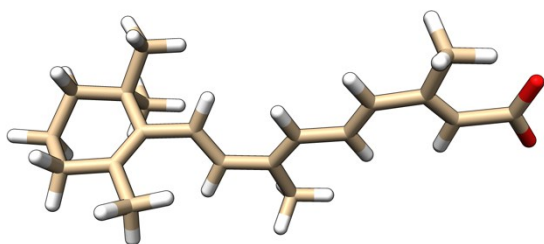
Conformation 15: -228.37



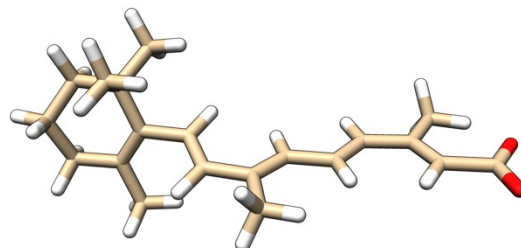
Conformation 7: -228.20



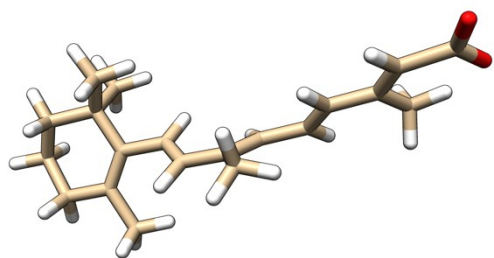
Conformation 6: -228.19



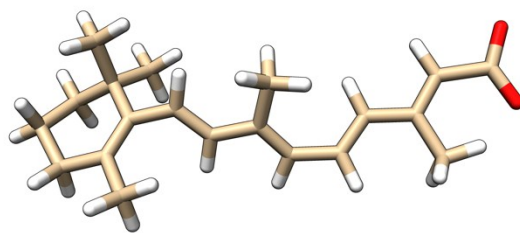
Conformation 11: -227.22



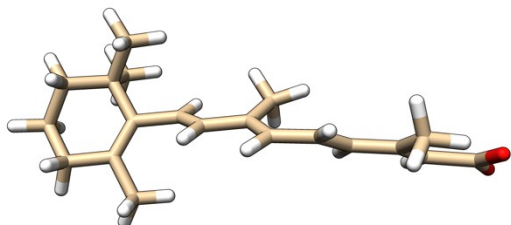
Conformation 10: -227.21



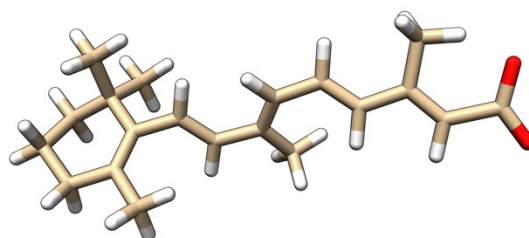
Conformation 17: -222.50



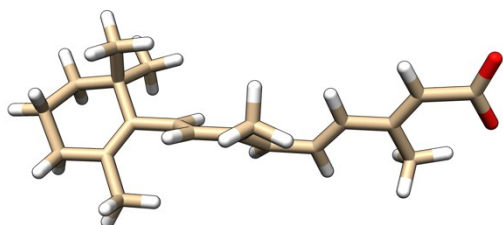
Conformation 19: -222.03



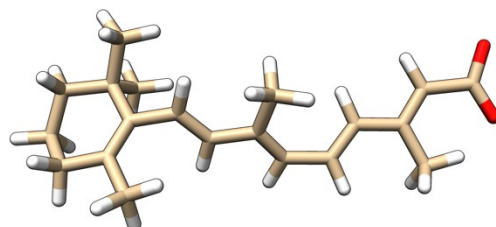
Conformation 32: -221.79



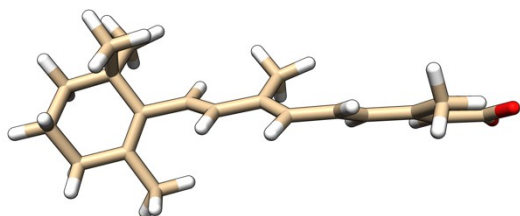
Conformation 18: -221.65



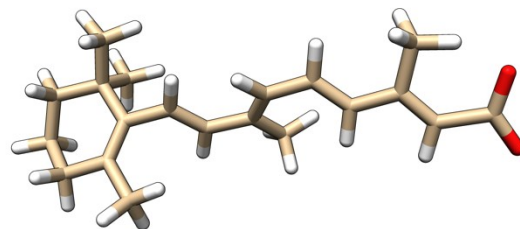
Conformation 26: -221.62



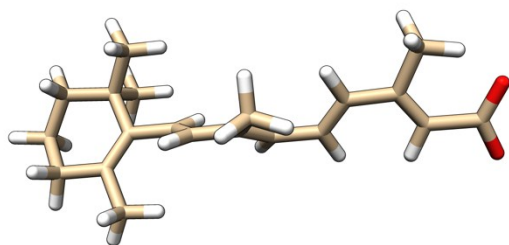
Conformation 23: -221.24



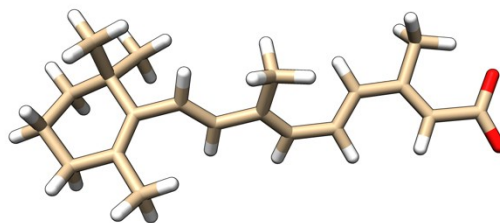
Conformation 28: -221.14



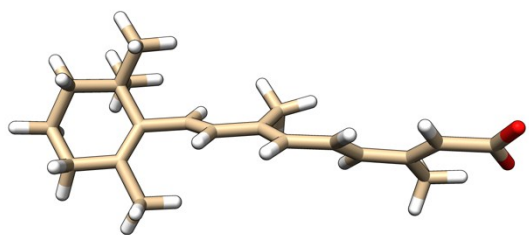
Conformation 21: -220.68



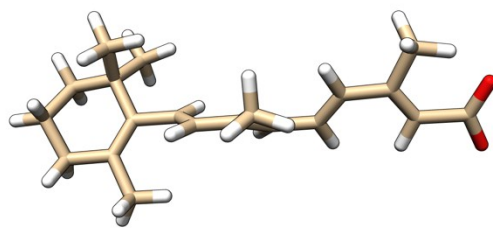
Conformation 20: -219.48



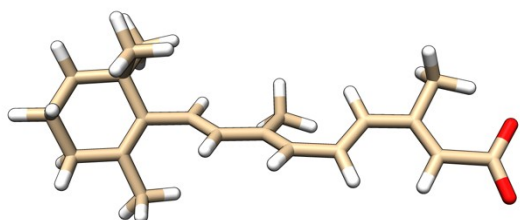
Conformation 24: -219.47



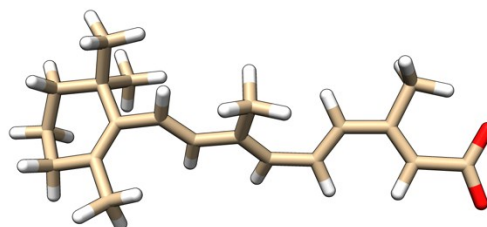
Conformation 25: -219.08



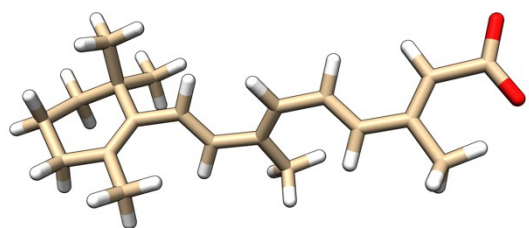
Conformation 27: -218.63



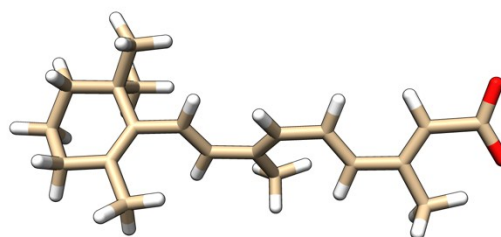
Conformation 31: -218.62



Conformation 29: -218.60

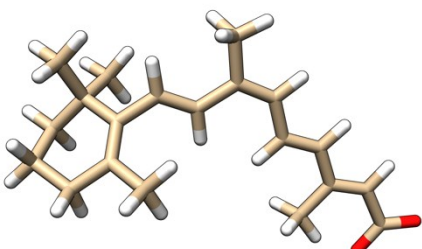
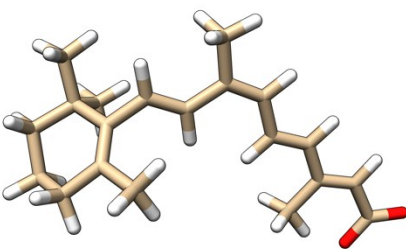
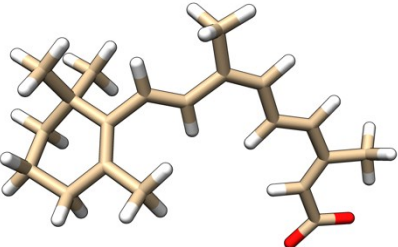
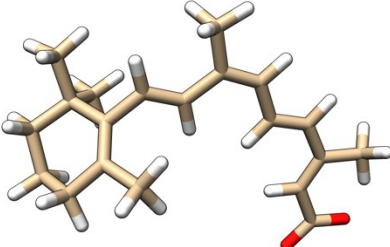
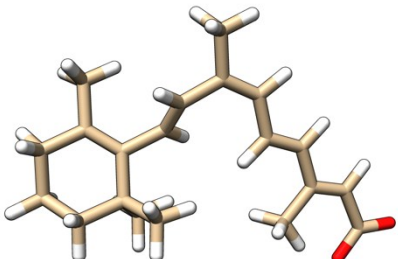
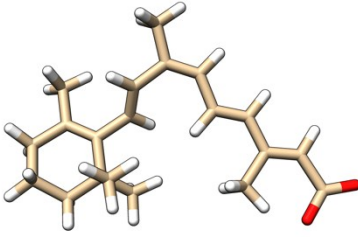
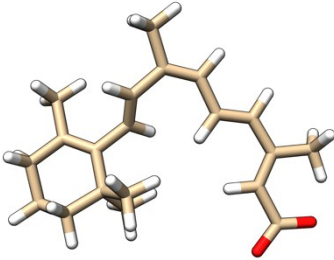
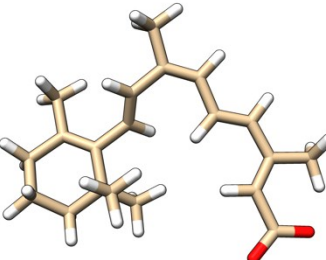


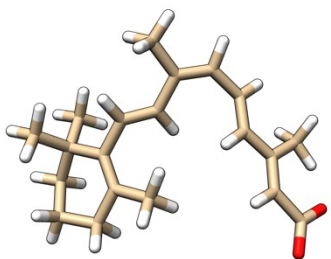
Conformation 22: -218.58



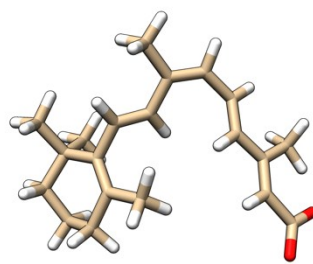
Conformation 30: -217.75 (highest)

Table 2: Conformer distribution of 9CRA in order of lowest energy. Distribution was calculated using the AM1 forcefield, and energies are shown from this calculation. The results were further validated at a higher level of theory (HF, STO-3G), and no obvious differences were exhibited. Energies are expressed in kJ/mol, and were calculated using Spartan 14. Each of these calculated conformations was used as a starting point for the docking process.

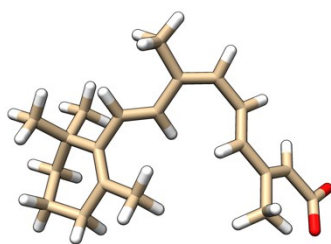
 <p>Conformation 1: -365.64 (lowest)</p>	 <p>Conformation 2: -364.41</p>
 <p>Conformation 3: -364.18</p>	 <p>Conformation 4: -363.12</p>
 <p>Conformation 5: -362.85</p>	 <p>Conformation 6: -362.69</p>
 <p>Conformation 7: -571840.30</p>	 <p>Conformation 8: -360.31</p>



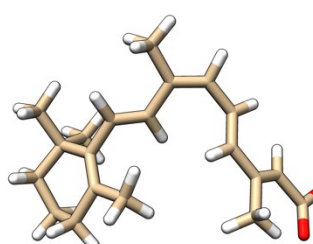
Conformation 9: -359.64



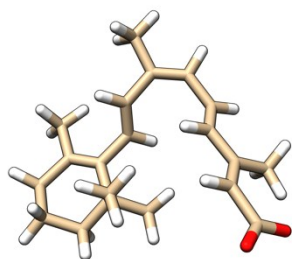
Conformation 10: -358.90



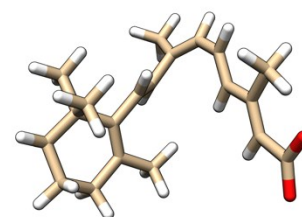
Conformation 11: -358.46



Conformation 12: -357.87



Conformation 13: -350.08



Conformation 14: -347.19 (highest)

Table 3: Conformer distribution of EC23 in order of lowest energy. Distribution was calculated using the AM1 forcefield, and energies are shown from this calculation. The results were further validated at a higher level of theory (HF, STO-3G), and no obvious differences were exhibited. Energies are expressed in kJ/mol, and were calculated using Spartan 14. This calculated conformation was used as a starting point for the docking process.

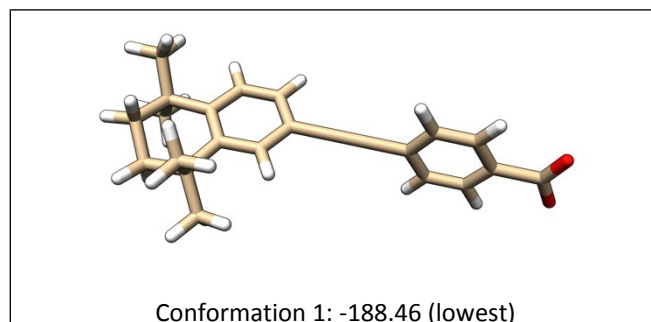


Table 4: Conformer distribution of EC19 in order of lowest energy. Distribution was calculated using the AM1 forcefield, and energies are shown from this calculation. The results were further validated at a higher level of theory (HF, STO-3G), and no obvious differences were exhibited. Energies are expressed in kJ/mol, and were calculated using Spartan 14. This calculated conformation was used as a starting point for the docking process.

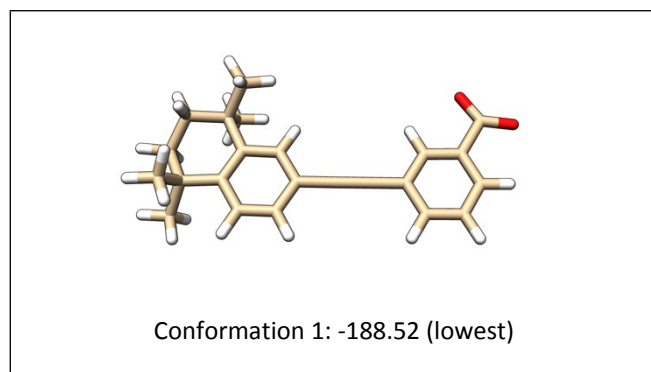


Table 5: Conformer distribution of EC23Me in order of lowest energy. Distribution was calculated using the AM1 forcefield, and energies are shown from this calculation. The results were further validated at a higher level of theory (HF, STO-3G), and no obvious differences were exhibited. Energies are expressed in kJ/mol, and were calculated using Spartan 14. Each of these calculated conformations was used as a starting point for the docking process.

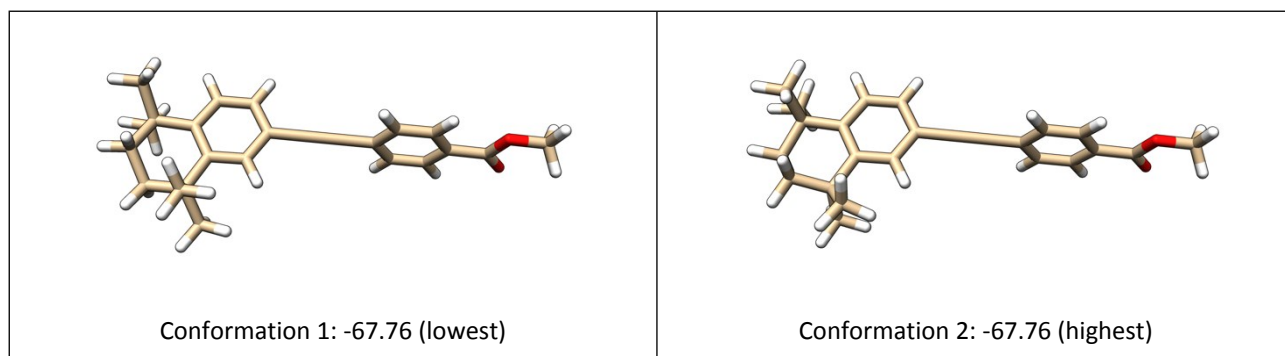
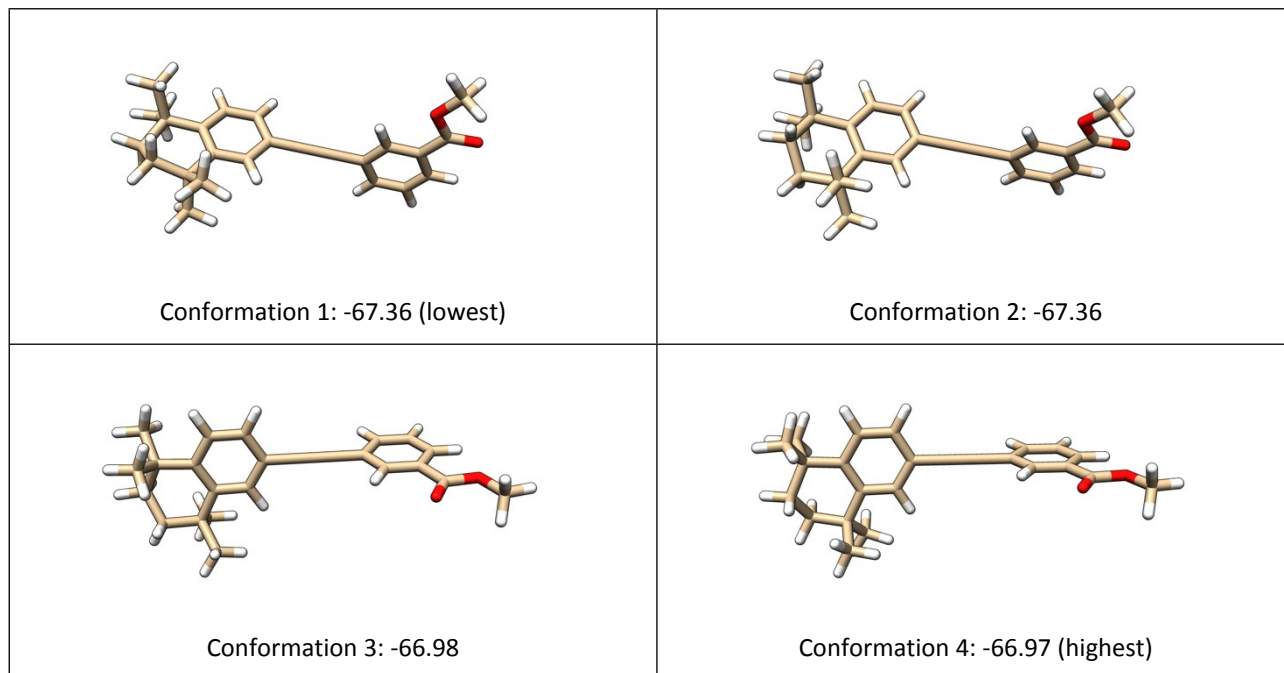


Table 6: Conformer distribution of EC19Me in order of lowest energy. Distribution was calculated using the AM1 forcefield, and energies are shown from this calculation. The results were further validated at a higher level of theory (HF, STO-3G), and no obvious differences were exhibited. Energies are expressed in kJ/mol, and were calculated using Spartan 14. Each of these calculated conformations was used as a starting point for the docking process.



Statistical analysis of ATRA docking conformation clustering

When the docking solutions from all 32 starting conformations of ATRA were analysed, it was noticed that they could be assigned into 11 different docked conformations. Each solution was therefore individually examined and assigned to one of these docked conformations, and the resultant clusters are shown in Table 7. To determine whether the distributions of each docked conformation were distinct for each RAR, a Fisher's Exact Test for Count Data with simulated P value based on 2000 replicates (using R version 3.1.2) was used to analyse Table 7. The P value for independence of rows and columns (null hypothesis of no independence) was < 0.001 for data altogether, or testing RAR α versus RAR β , RAR α versus RAR γ and RAR β versus RAR γ . Each conformational distribution is therefore different, and significant after Bonferroni correction for experiment-wise P value.

ATRA Docked Conformation	Selection frequency		
	RAR α	RAR β	RAR γ
1	110	96	92
2	58	17	18
3	3	2	0
4	17	15	0
5	0	1	1
6	4	12	0
7	18	52	50
8	12	4	9
9	0	7	1
10	0	12	4
11	0	5	10
	Total = 222	Total = 223	Total = 185

Table 7: Clustering of the docked conformations of ATRA in RAR α , RAR β and RAR γ .

Additional hydrophobic interaction images

Figures highlighting the possible hydrophobic interactions with the highest scoring binding poses of the retinoids with RAR α ⁵, RAR β ⁶ and RAR γ ⁷ were produced using GOLD,⁸ and visualised with UCSF Chimera.⁹

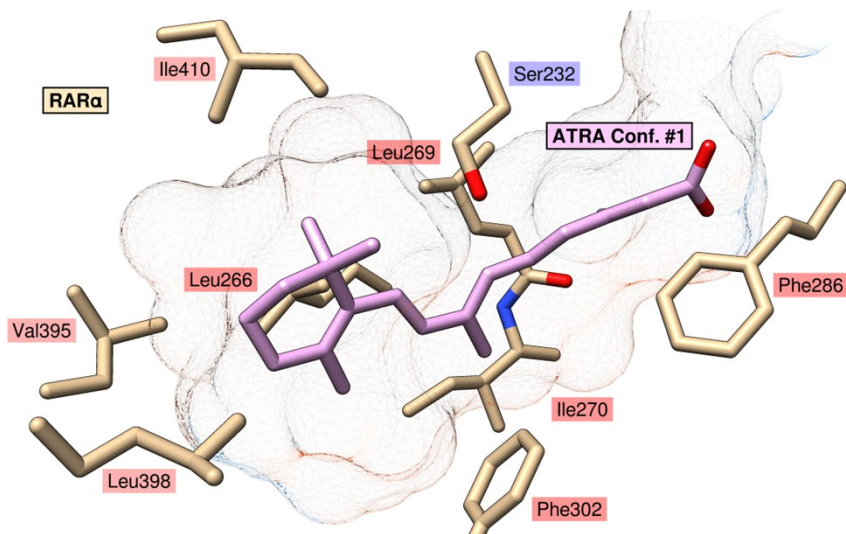


Figure 3: Hydrophobic interactions with the highest scoring binding pose of ATRA conformation 1 in RAR α .

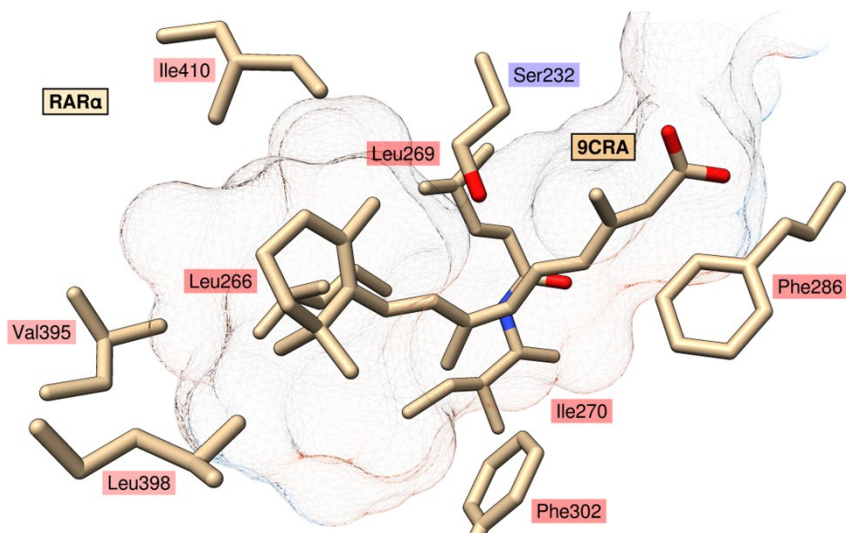


Figure 4: Hydrophobic interactions with the highest scoring binding pose of 9CRA in RAR α .

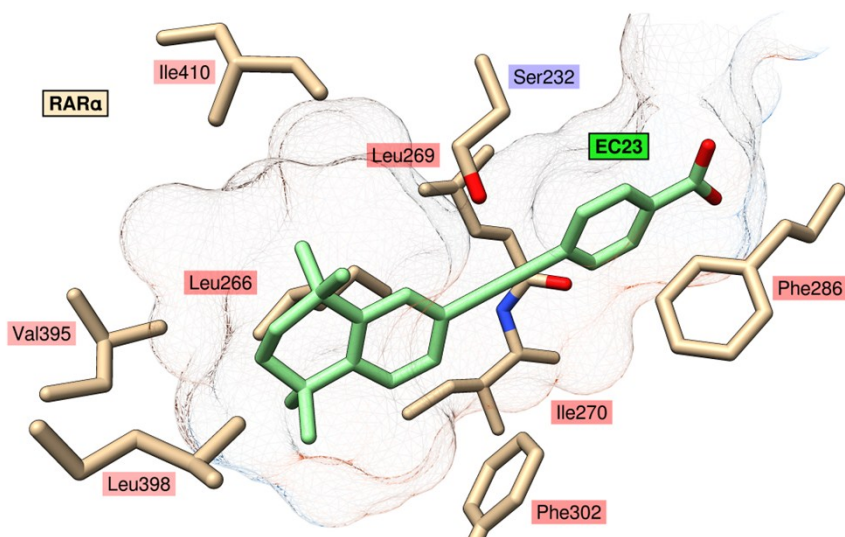


Figure 5: Hydrophobic interactions with the highest scoring binding pose of EC23 in RAR α .

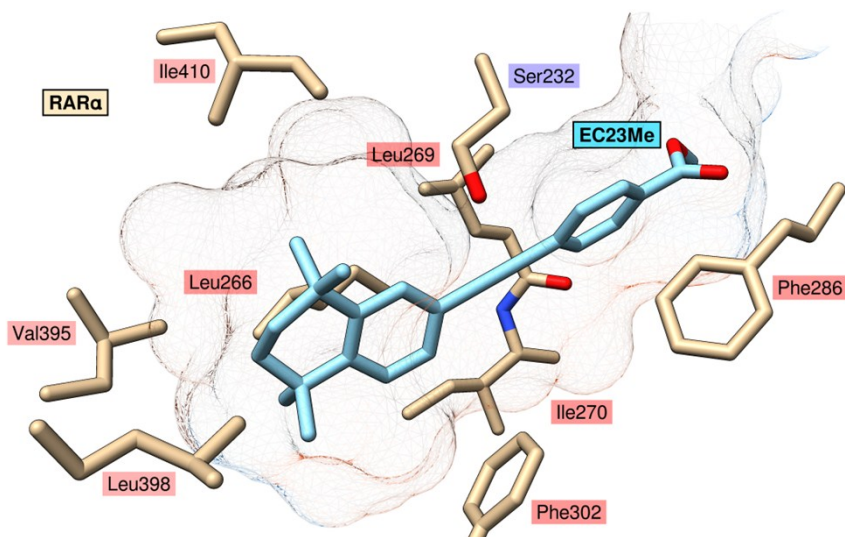


Figure 6: Hydrophobic interactions with the highest scoring binding pose of EC23Me in RAR α .

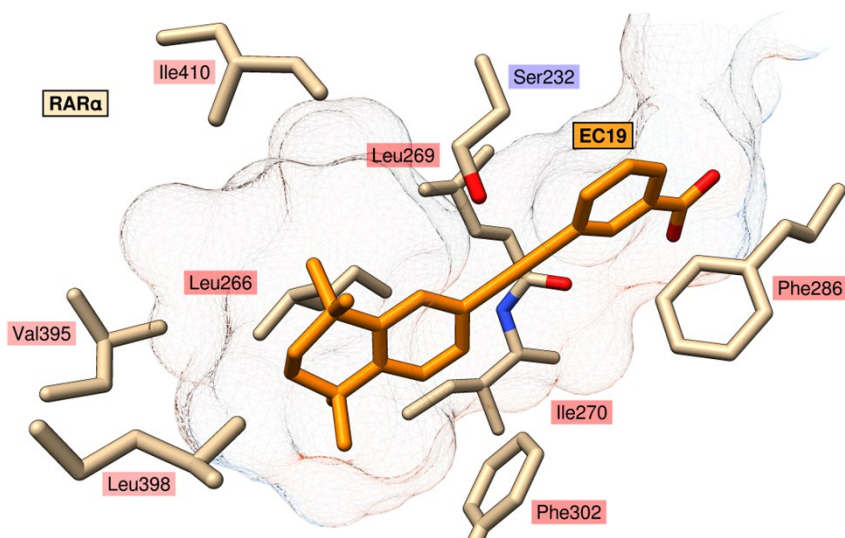


Figure 7: Hydrophobic interactions with the highest scoring binding pose of EC19 in RAR α .

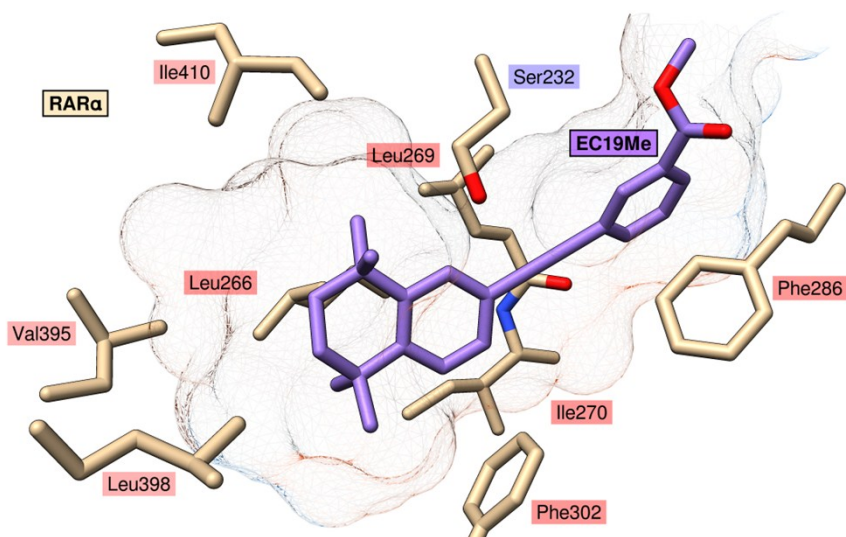


Figure 8: Hydrophobic interactions with the highest scoring binding pose of EC19Me in RAR α .

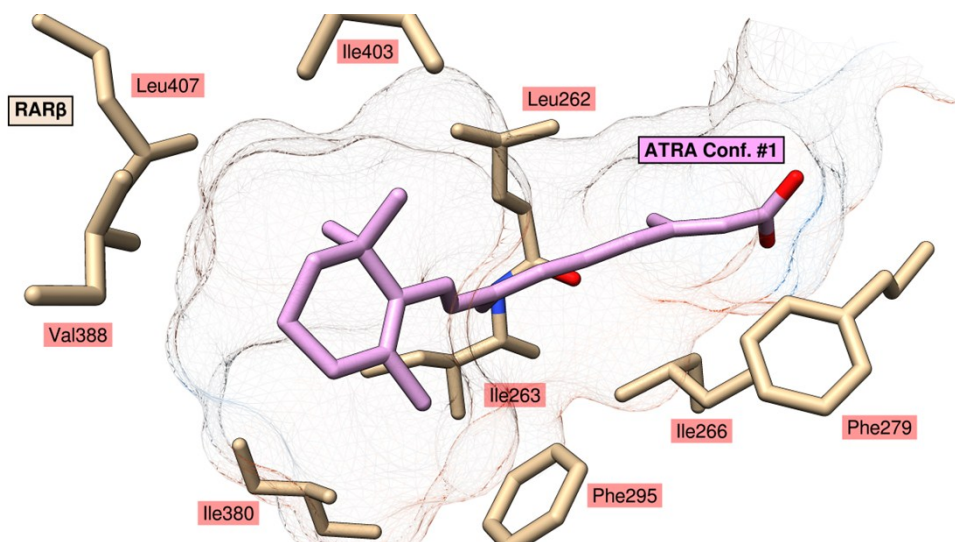


Figure 9: Hydrophobic interactions with the highest scoring binding pose of ATRA conformation 1 in RAR β .

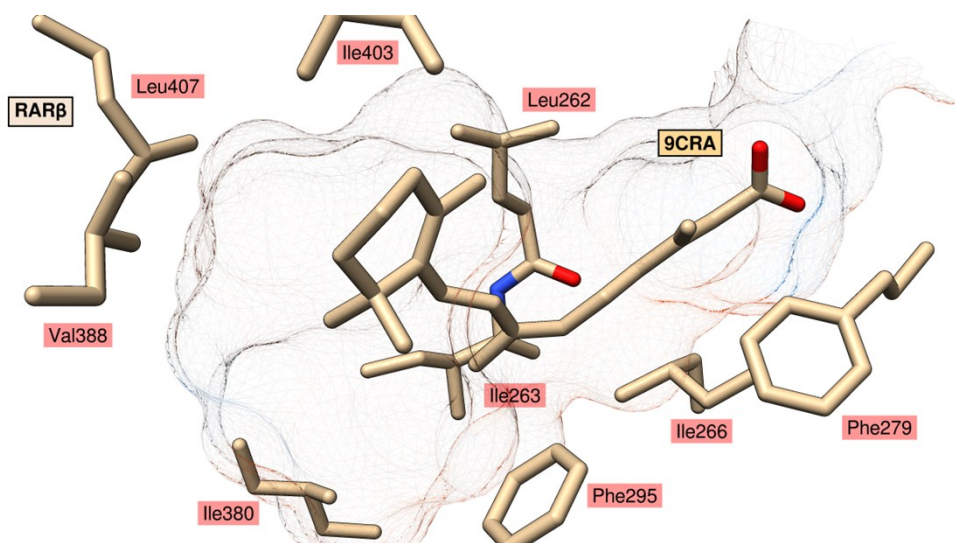


Figure 10: Hydrophobic interactions with the highest scoring binding pose of 9CRA in RAR β .

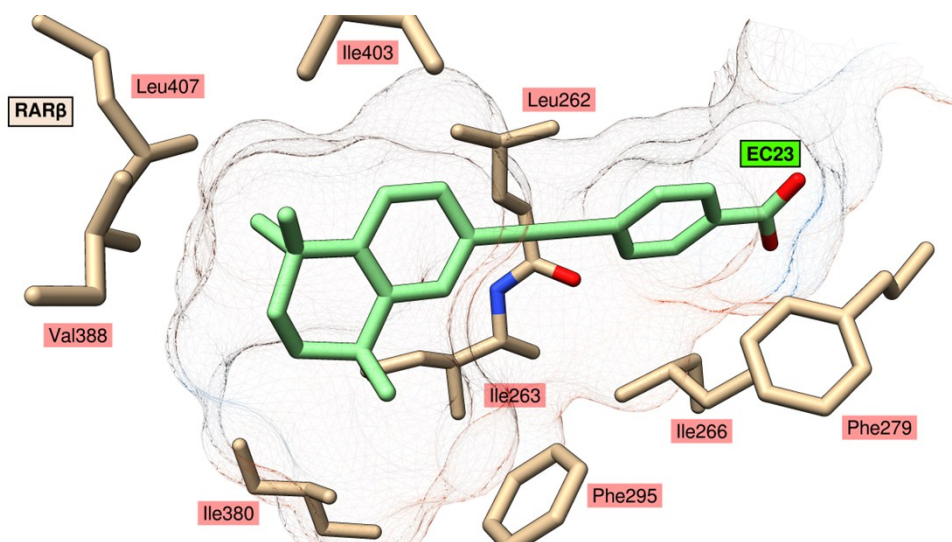


Figure 11: Hydrophobic interactions with the highest scoring binding pose of EC23 in RAR β .

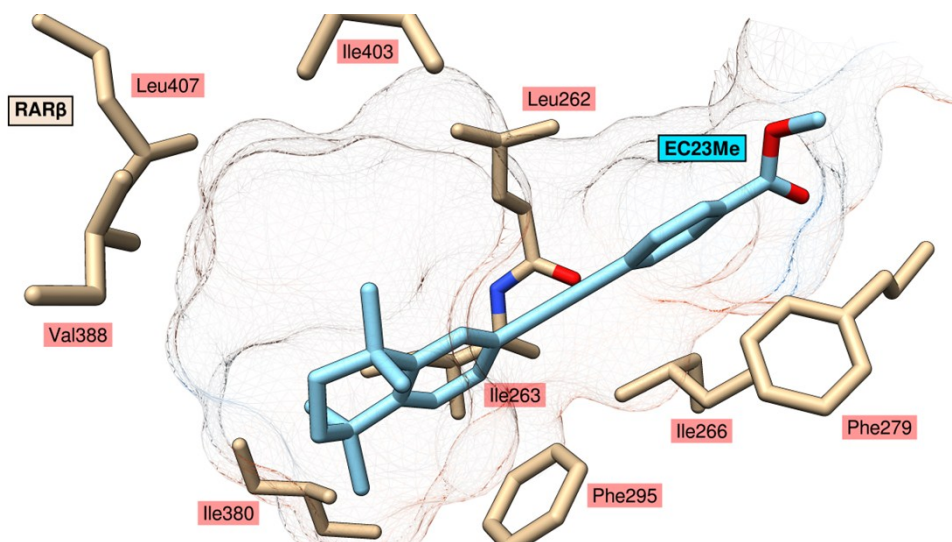


Figure 12: Hydrophobic interactions with the highest scoring binding pose of EC23Me in RAR β .

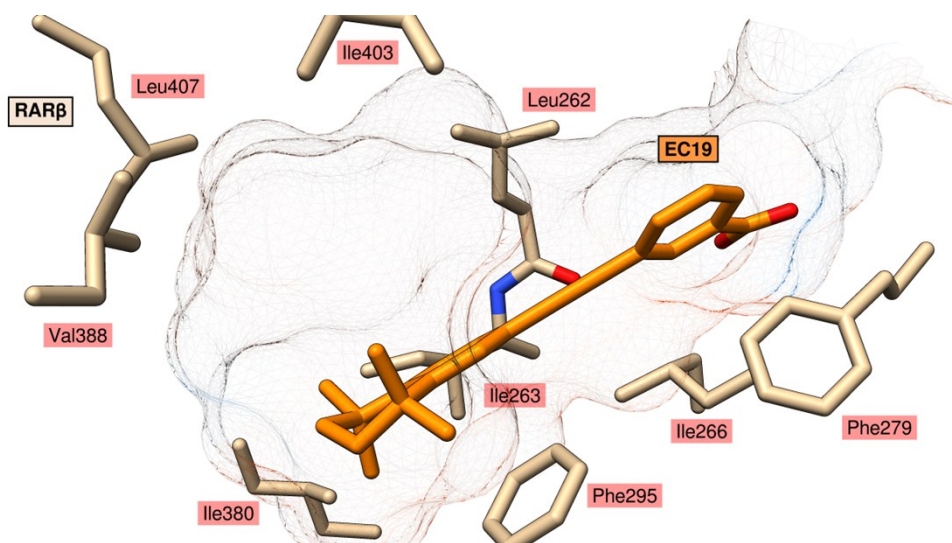


Figure 13: Hydrophobic interactions with the highest scoring binding pose of EC19 in RAR β .

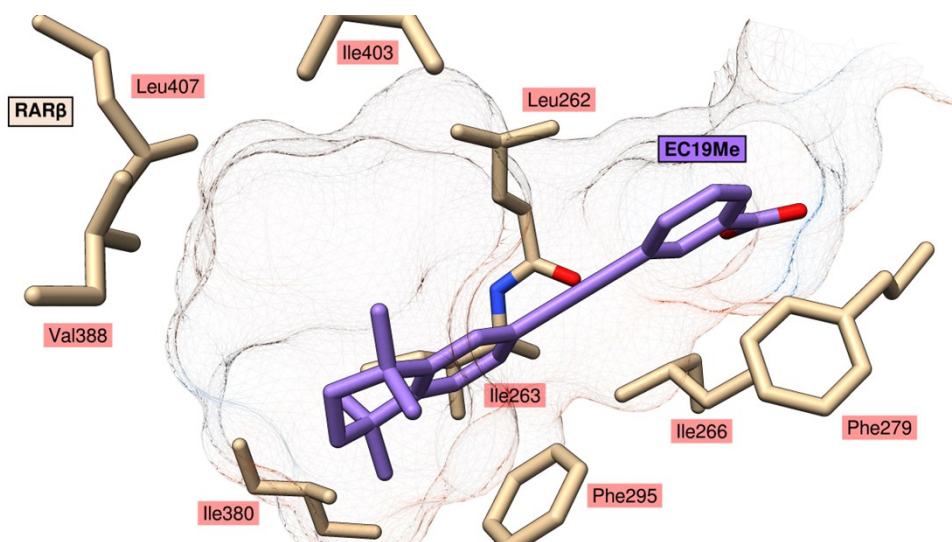


Figure 14: Hydrophobic interactions with the highest scoring binding pose of EC19Me in RAR β .

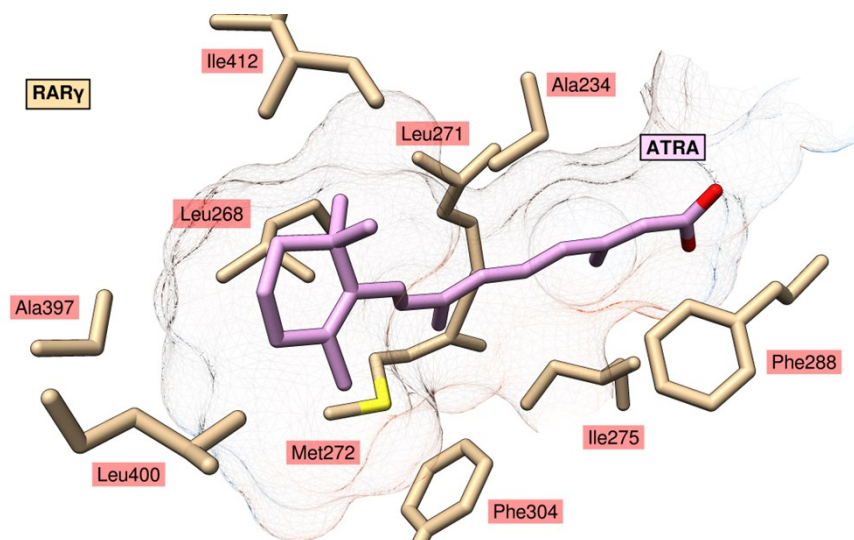


Figure 15: Hydrophobic interactions with the highest scoring binding pose of ATRA conformation 1 in RAR γ .

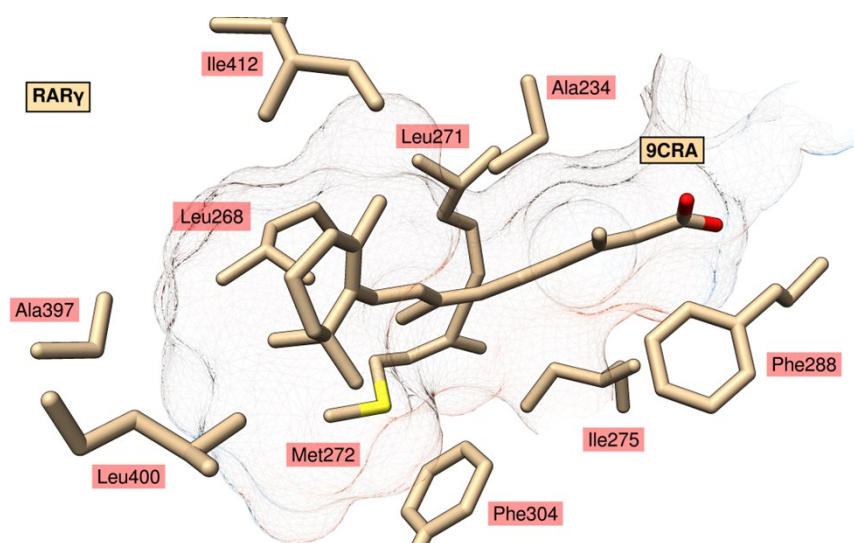


Figure 16: Hydrophobic interactions with the highest scoring binding pose of 9CRA in RAR γ .

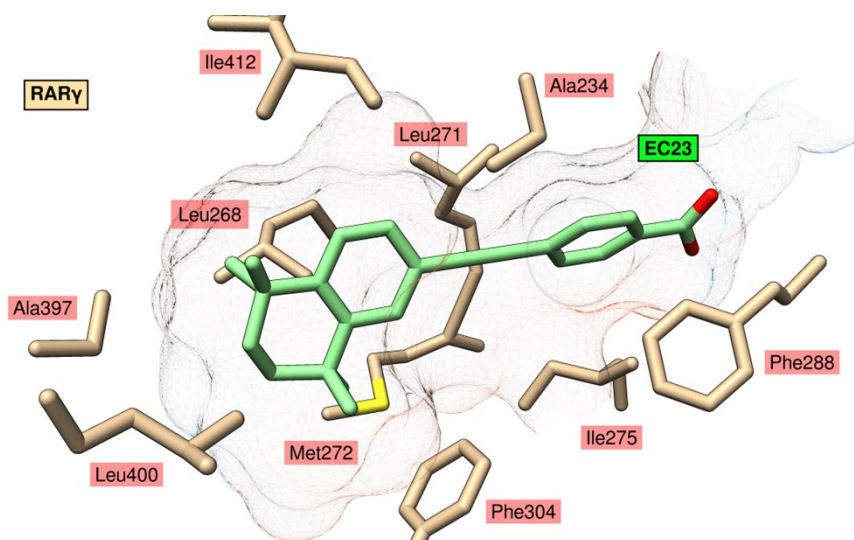


Figure 17: Hydrophobic interactions with the highest scoring binding pose of EC23 in RARγ.

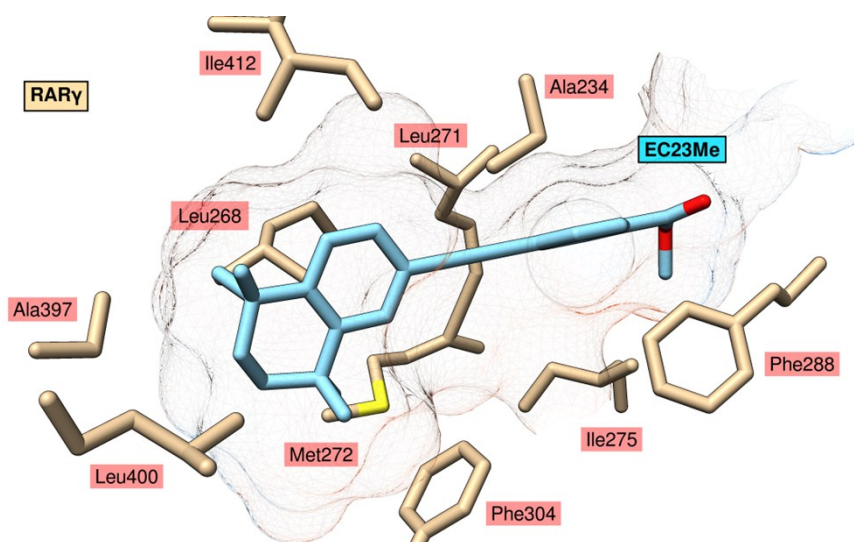


Figure 18: Hydrophobic interactions with the highest scoring binding pose of EC23Me in RARγ.

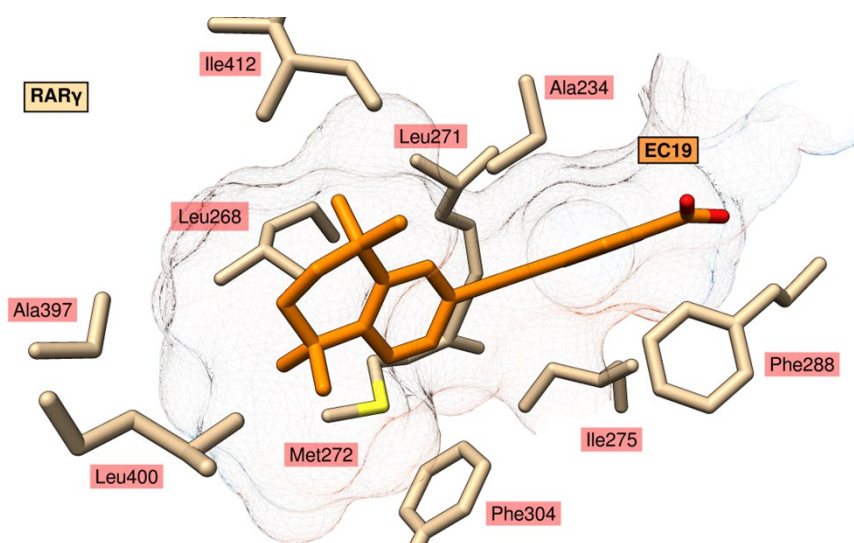


Figure 19: Hydrophobic interactions with the highest scoring binding pose of EC19 in RARγ.

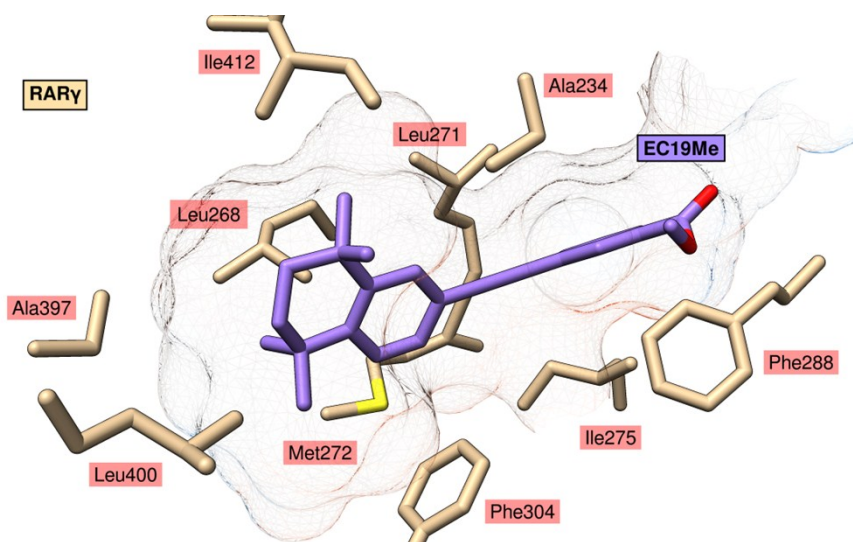


Figure 20: Hydrophobic interactions with the highest scoring binding pose of EC19Me in RARy.

Additional hydrogen bonding interaction images

Figures highlighting the possible hydrogen bonding interactions with the highest scoring binding poses of the retinoids with RAR β ⁶ and RAR γ ⁷ were produced using GOLD,⁸ and visualised with UCSF Chimera.⁹

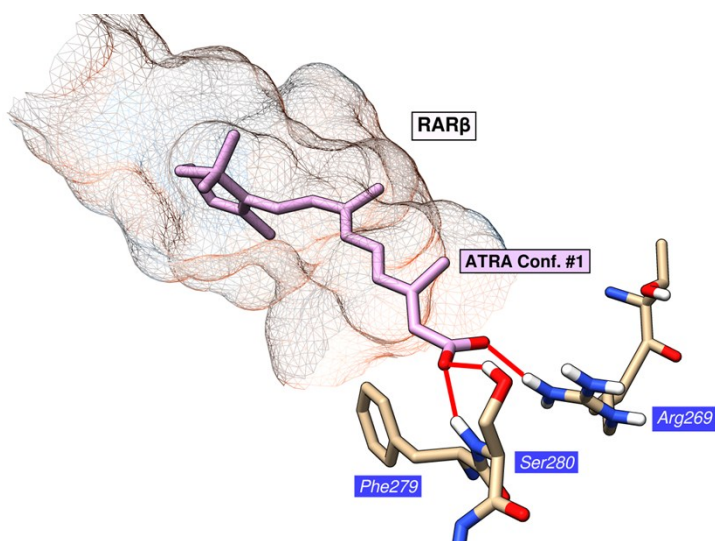


Figure 21: Hydrogen bonding interactions with the highest scoring binding pose of ATRA in RAR β .

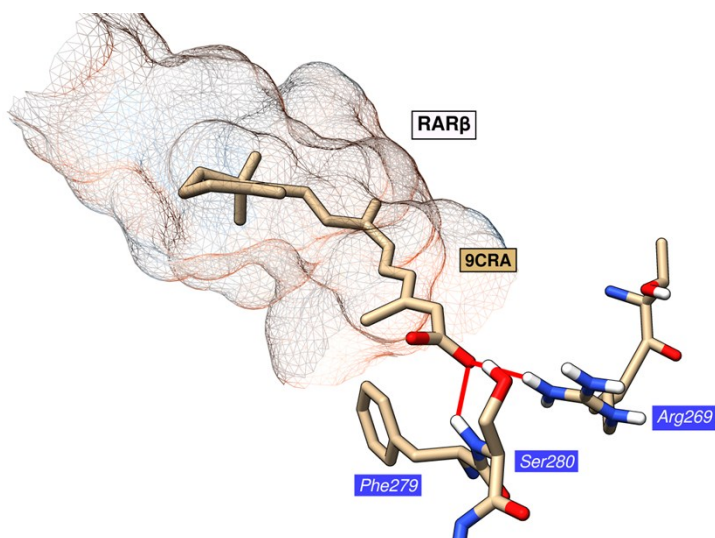


Figure 22: Hydrogen bonding interactions with the highest scoring binding pose of 9CRA in RAR β .

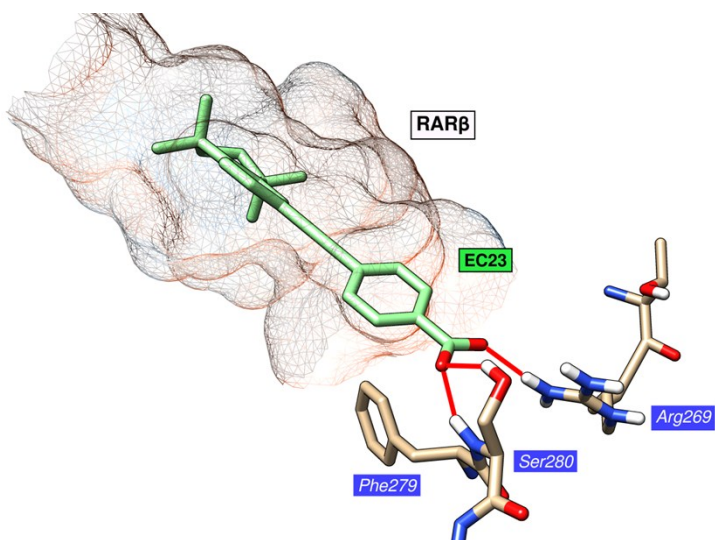


Figure 23: Hydrogen bonding interactions with the highest scoring binding pose of EC23 in RAR β .

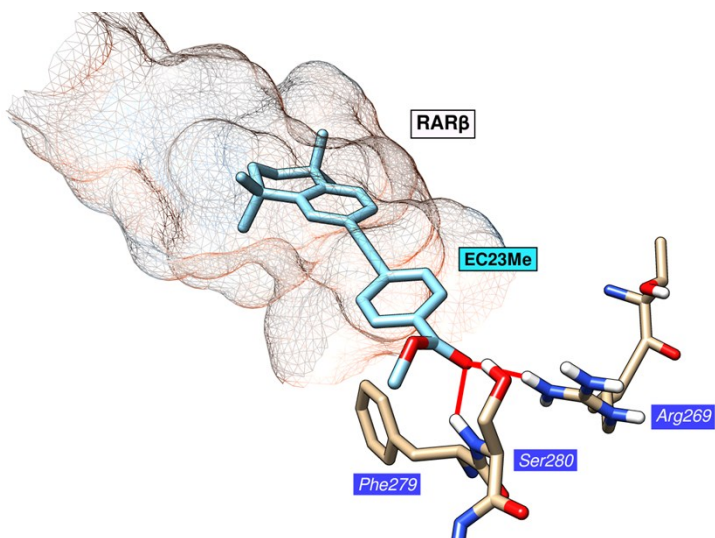


Figure 24: Hydrogen bonding interactions with the highest scoring binding pose of EC23Me in RAR β .

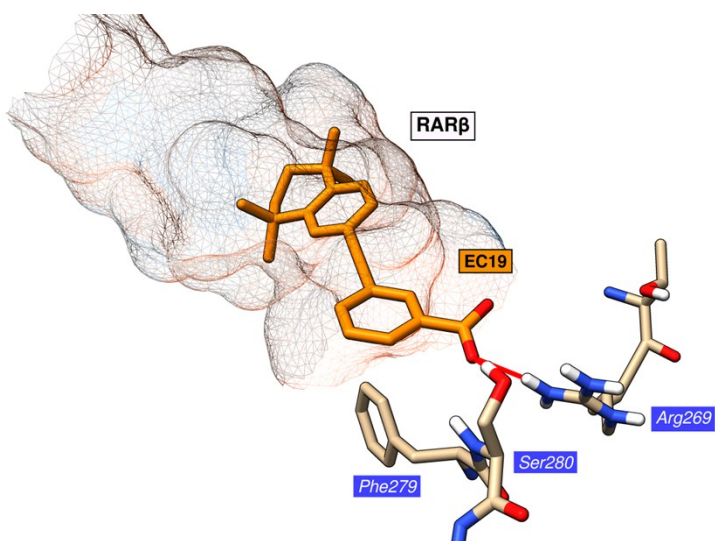


Figure 25: Hydrogen bonding interactions with the highest scoring binding pose of EC19 in RAR β .

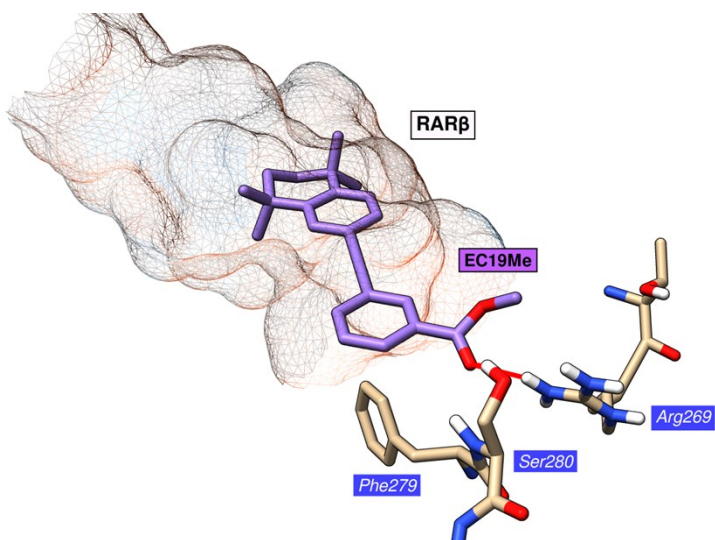


Figure 26: Hydrogen bonding interactions with the highest scoring binding pose of EC19Me in RARβ.

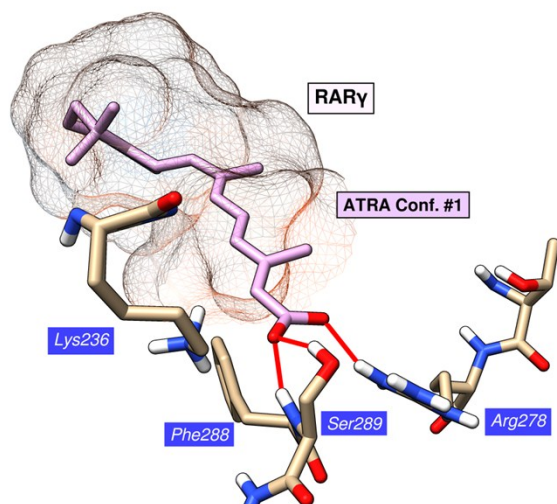


Figure 27: Hydrogen bonding interactions with the highest scoring binding pose of ATRA in RARγ.

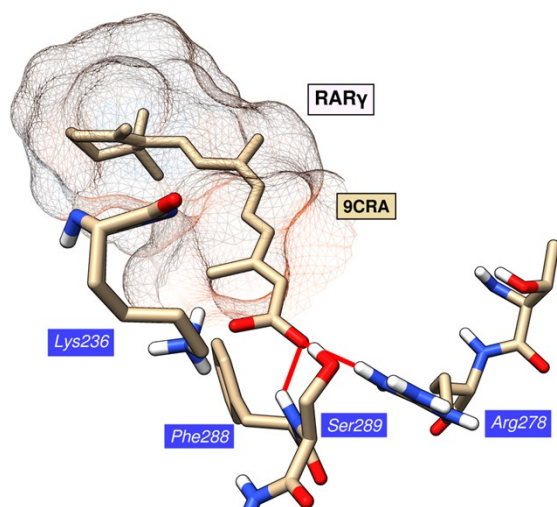


Figure 28: Hydrogen bonding interactions with the highest scoring binding pose of 9CRA in RARγ.

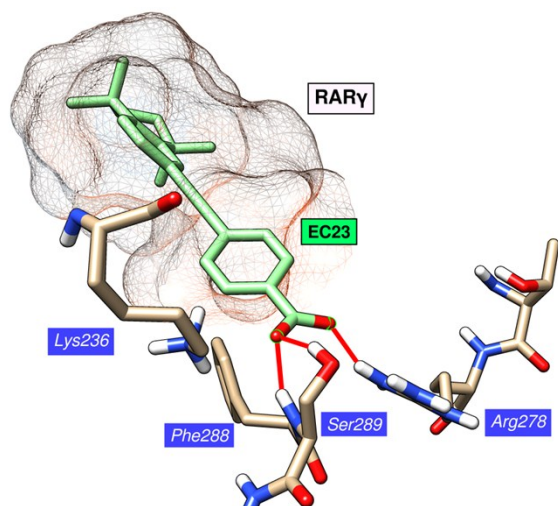


Figure 29: Hydrogen bonding interactions with the highest scoring binding pose of EC23 in RAR γ .

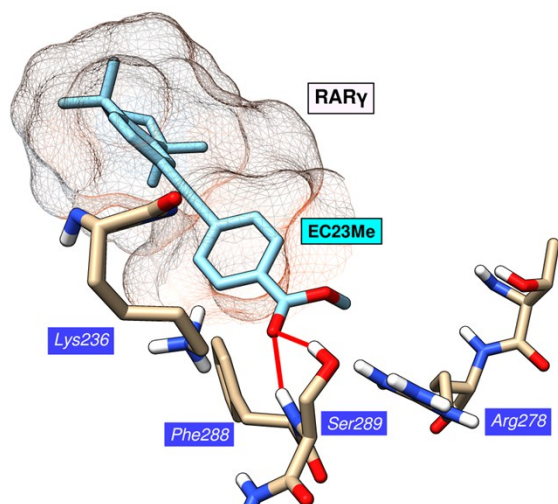


Figure 30: Hydrogen bonding interactions with the highest scoring binding pose of EC23Me in RAR γ .

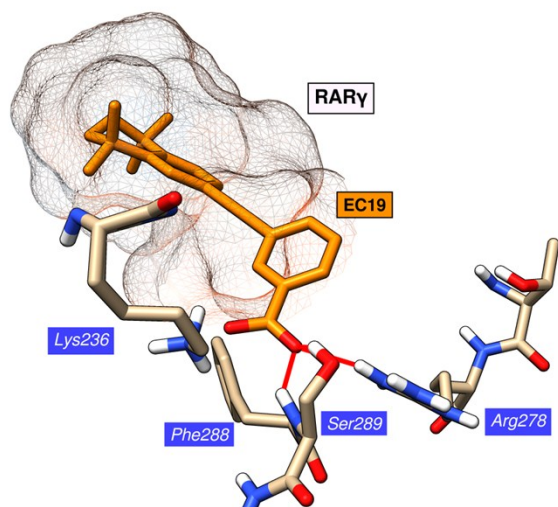


Figure 31: Hydrogen bonding interactions with the highest scoring binding pose of EC19 in RAR γ .

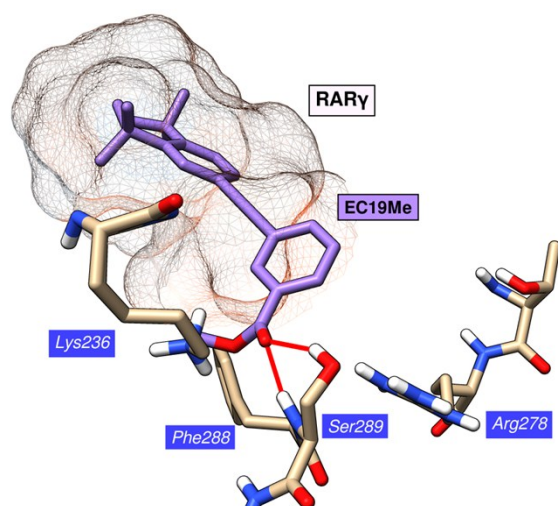


Figure 32: Hydrogen bonding interactions with the highest scoring binding pose of EC19Me in RAR γ .

References

- 1 S. Hoops, S. Sahle, R. Gauges, C. Lee, J. Pahle, N. Simus, M. Singhal, L. Xu, P. Mendes and U. Kummer, *Bioinformatics*, 2006, **22**, 3067–3074.
- 2 P. Waage and C. M. Gulberg, *J. Chem. Educ.*, 1986, **63**, 1044.
- 3 K. C. Kwok and N. H. Cheung, *Anal. Chem.*, 2010, **82**, 3819–3825.
- 4 D. N. Lavery and I. J. McEwan, *Biochemistry*, 2008, **47**, 3352–3359.
- 5 A. le Maire, C. Teyssier, C. Erb, M. Grimaldi, S. Alvarez, A. R. de Lera, P. Balaguer, H. Gronemeyer, C. A. Royer, P. Germain and W. Bourguet, *Nat. Struct. Mol. Biol.*, 2010, **17**, 801–807.
- 6 P. Germain, S. Kammerer, E. Pérez, C. Peluso-Iltis, D. Tortolani, F. C. Zusi, J. Starrett, P. Lapointe, J. Daris, A. Marinier, A. R. de Lera, N. Rochel and H. Gronemeyer, *EMBO Rep.*, 2004, **5**, 877–882.
- 7 J. P. Renaud, N. Rochel, M. Ruff and V. Vivat, *Nature*, 1995, **378**, 681–689.
- 8 G. Jones, P. Willett, R. C. Glen, A. R. Leach and R. Taylor, *J. Mol. Biol.*, 1997, **267**, 727–748.
- 9 E. F. Pettersen, T. D. Goddard, C. C. Huang, G. S. Couch, D. M. Greenblatt, E. C. Meng and T. E. Ferrin, *J. Comput. Chem.*, 2004, **25**, 1605–1612.